Extent of Excess Far-Infrared Emission around Luminosity Class III Stars

S. Kim – University of California
B. Zuckerman – University of California
M. Silverstone – University of California

Citation of published version:

Kim, S., Zuckerman, B., Silverstone, M. (2001): Extent of Excess Far-Infrared Emission around Luminosity Class III Stars. *The Astronomical Journal,* 550(2).
DOI: https://doi.org/10.1086/319803

THE ASTROPHYSICAL JOURNAL, 550:1000–1006, 2001 April 1

EXTENT OF EXCESS FAR-INFRARED EMISSION AROUND LUMINOSITY CLASS III STARS

SUNGSOO S. KIM, B. ZUCKERMAN, AND MURRAY SILVERSTONE[1]
Division of Astronomy and Astrophysics, University of California, Los Angeles, CA 90095-1562;
sskim@astro.ucla.edu, ben@astro.ucla.edu, murray@as.arizona.edu
Received 2000 August 28; accepted 2000 November 30

ABSTRACT

With the *Infrared Space Observatory*, we conducted 3 × 3 pixel imaging photometry of 12 luminosity class III stars, which were previously presumed to have dust particles around them, at far-infrared wavelengths (60 and 90 μm). Eleven out of 12 targets show a peak of excess (above photosphere) far-infrared emission at the location of the star, implying that the dust particles are truly associated with stars. To estimate the size of the excess emission source, the flux ratio of center to boundary pixels of the 3 × 3 array was examined. The radius of the dust emission is found to be ~3000 to ~10,000 AU for a thin shell distribution and ~5000 to ~25,000 AU for a uniform distribution. We consider three models for the origin of the dust: disintegration of comets, sporadic dust ejection from the star, and emission from nearby interstellar cirrus. The data seem to rule out the first model (as far as the "Kuiper belt–like" particles are assumed to be large blackbody grains) but do not enable us to choose between the other two models.

Subject headings: circumstellar matter — infrared: stars — stars: late-type

1. INTRODUCTION

Zuckerman, Kim, & Liu (1995) correlated the Bright Star Catalogue (Hoffleit & Warren 1991) and the Michigan Spectral Catalogue (Houk, Cowley, & Smith-Moore 1975-1988) with the *IRAS* catalogs to determine which, if any, luminosity class III giant stars (first-ascent red giants) have associated circumstellar dust particles that radiate at far-infrared (far-IR) wavelengths. Of more than 40,000 class III giant stars in the two catalogs, they found that perhaps 300 have associated dust.

The presence of particulate material near pre–main-sequence, main-sequence, asymptotic giant branch, and supergiant stars may be accounted for in rather straightforward ways (remnants from the star formation for the former two and mass loss for the latter two). But, there is no obvious way to produce and retain large amounts of dust near first-ascent giant stars, which are thought to be too old to still possess much leftover material and insufficiently evolved to have lost a significant amount of their mass. However, one may conjecture that the presence of dust around first-ascent giants may involve one or more of the following phenomena: mass loss, binarity, planetary systems, and evaporation of Kuiper belt material. Recently, Jura (1999) has analyzed three models for the dust around eight first-ascent giant stars: orbiting dust resulting from the disintegration of comets located in extrasolar analogs of the Kuiper belt, dust sporadically ejected from the star, and emission from particles in the interstellar medium that are accidentally near the star, the "cirrus hot spot."

Among the Zuckerman et al. (1995) list of 100, we observed 12 first-ascent giant stars with the PHOT instrument of the *Infrared Space Observatory* (*ISO*)[2] to determine if the excess far-IR emission is truly associated with the stars and to estimate the size of the region that produces the excess far-IR emission.

Section 2 describes our *ISO* observations and data reduction. Section 3 discusses the data analysis, including the determination of the size of the far-IR excess source. Section 4 then compares our results with Jura's models. A summary is given in § 5.

2. OBSERVATIONS AND DATA REDUCTION

The target stars were observed with the C100 camera of the ISOPHOT instrument using filters 60 ($\lambda_c = 60.8$ μm, $\Delta\lambda = 23.9$ μm) and 90 ($\lambda_c = 95.1$ μm, $\Delta\lambda = 51.4$ μm). C100 is a 3 × 3 Ge:Ga pixel array. The sky coverage of each pixel is 43″.5 × 43″.5 and the gap between adjacent pixels corresponds to 2″.5 on the sky. The diffraction limit of the ISO is 25″ at 60 μm and 38″ at 90 μm. Observation mode PHT37-39 was used to obtain a sequence of "dark-off1-on-off2" measurements for each target and filter. The target was measured at the "on" sequence position and, to obtain the background intensity around the target, two off-position measurements ("off1" and "off2") were made at a single position 2′.5 closer to the nearer celestial pole than the target. Calibration measurements were performed at the "dark" and "off2" sequence positions using the Fine Calibration Source 1 (FCS1) on board the satellite. The integration time was 64 s for scientific measurements (target and background) and 32 s for FCS1 measurements.

The data were reduced using the PHOT interactive analysis software package (PIA; Gabriel et al. 1997) version 7.2.2(e). Each measurement consisted of 64 ramps (16 for FCS1), and each ramp has 31 nondestructive readouts (63 for FCS1) and one destructive readout. Data reductions described below used the default values of the PIA except when specified. Nonlinearity correction and two-threshold deglitching were applied to each ramp, and a linear fit was made to the ramp to derive the signals in volts per second. These signals were deglitched again using the minmax clipping algorithm with a threshold set at 2.4 σ. Then reset interval correction and dark current subtraction were applied to the signals.

The responsivity of the system, that is, the conversion of signal (volts per second) to flux (janskys), was obtained by

[1] Present address: Steward Observatory, University of Arizona, Tucson, AZ 85721.

[2] *ISO* is an ESA project with instruments funded by ESA member states (especially the PI countries: France, Germany, The Netherlands, and the United Kingdom) and with the participation of ISAS and NASA.

time interpolating two FCS1 measurements for each target. At each star the background at each of the nine pixels was obtained from an average of the "off1" and "off2" images. Inspection of the 60 μm background fluxes obtained in this way at the 12 target stars indicated a larger flux (by 10%) at the central pixel of the background; this difference between central and boundary pixels is larger than the spatial variation of the background. We interpret the difference as due to a bias in the FCS1 signal and correct for it as follows: The flux of each "on" pixel is divided by the background flux of the corresponding pixel and multiplied by the average of the 9 pixel background flux. This background average is then subtracted from the "on" pixel flux to produce a measure of the source flux.

To check the accuracy of data measurement and reduction, our *ISO* background average and the 4′ *IRAS* Sky Survey Atlas background (before the subtraction of a zodiacal model) were compared. Figure 1 shows that the two flux values agree very well.

The uncertainty for the background flux was estimated by taking the rms value of the nine differences between two "off" measurements of each pixel. The uncertainty for the total boundary-pixel flux of the source was estimated to be the square root of 4 times the sum of the variance of 4 crossing pixels and that of 4 diagonal pixels considering the point-symmetric nature of the point-spread function (PSF). Since only one pixel measurement is available for the central pixel of the source, we simply assume that background and central "on" pixel uncertainties are proportional to their fluxes. The average signal-to-noise ratio (S/N) is found to be $\sim$20 for background flux and $\sim$5 for central flux of the source and $\sim$2.2 for boundary-pixel flux of the source. However, our analysis involves the boundary-pixel flux of the source only in the context of a sum of eight boundary-pixel fluxes, which has an average S/N of $\sim$6.

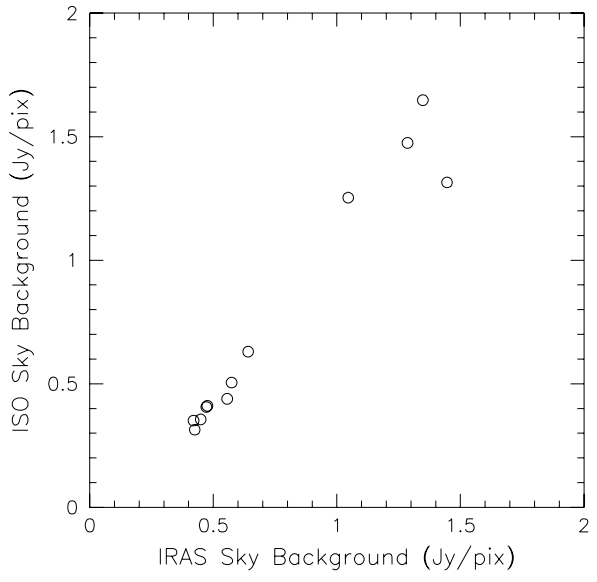

FIG. 1.—Comparison of 60 μm background flux observed by *IRAS* and *ISO* near our target stars. Fluxes are in units of janskys per 1 *ISO* C100 pixel area. *IRAS* flux is the 4′ *IRAS* Sky Survey Atlas background before subtraction of a zodiacal model. The mean of the difference between two data sets is 0.4%, and the standard deviation of the mean of the difference is 5%. The uncertainty in flux ranges from 2.2% to 4.8% for the *ISO* data and from 0.1% to 4.6% for the *IRAS* data (the *IRAS* uncertainty is from the cirrus confusion noise).

3. DATA ANALYSIS

Measured *ISO* fluxes are presented in Table 1 along with the *IRAS* fluxes. Since the fluxes are neither color-corrected nor compensated for their detector sizes and PSF shapes, the *ISO* and *IRAS* data are not to be compared directly.

3.1. *Association with Optical Counterparts*

Since the presumed optical counterparts are targeted at the central pixel of the 3×3 array, if the material responsible for excess far-IR emission is distributed around the star with an intensity concentration toward the center or with an extent smaller than one pixel size, the intensity of the central pixel in our *ISO* data should be highest. We find that the peak intensity is located at the central pixel for all stars except HD 221776, which has a 90 μm peak intensity at the boundary pixel to the south, and HD 24124, which has 60 and 90 μm peak intensities at the boundary pixel to the northwest. We have identified in the Digitized Sky Survey a galaxy-like object at the location of the 60 and 90 μm peak intensities of HD 24124. Since the peak intensity pixels at both passbands coincide with the nearby galaxy, we attribute to it the far-IR emission previously presumed to be associated with HD 24124. However, in the case of HD 221776, because no object was found near the position of the 90 μm peak intensity from the Digitized Sky Survey and because the 60 μm peak intensity occurs at the central pixel, we believe that the 60 μm peak intensity is truly associated with the star and the 90 μm peak intensity is not real or is due to an unidentified nearby object. In addition, the second brightest 90 μm pixel is the central one and the ratio of 60 to 90 μm fluxes is plausible for a real source located at the star.

The fact that the central pixel has the highest intensity for 11 out of 12 stars at 60 μm suggests that the far-IR *IRAS* sources truly are associated with most of the giant stars presented in Table 1 of Zuckerman et al. (1995).

3.2. *The Source Size*

A 3×3 array is too coarse to give information on the source size directly from its image. However, if the distribution of the emission source is simple and axisymmetric about the image center, the extent of the source may be inferred from the ratio (r) of the flux in the central pixel to the sum of the fluxes in the 8 boundary pixels (Table 1). When defining r, only excess (i.e., nonphotospheric) emission is considered. By comparing the measured flux ratio $r_{\rm obs}$ and a model flux ratio $r_{\rm mod}$, one may estimate the size of the extended source.

When calculating $r_{\rm mod}$, one first needs a footprint, which is the fraction of the energy in the PSF that falls onto a pixel as a function of the pixel's location relative to the center of the PSF. Then the fraction of the flux onto a certain pixel from an extended emission source is obtained by convolving the footprint with an assumed source distribution. The PIA package includes model footprints of the ISOPHOT C100 camera, but a recent footprint calibration by Laureijs shows that the observed footprints for the whole array at a few different locations are slightly smaller than the PIA model values.[3] While the PIA model gives the full two-dimensional footprint, the calibration by Laureijs gives

[3] Laureijs, R. J. 1999, Point-Spread Function Fractions Related to the ISOPHOT C100 and C200 Arrays. Available at URL http://isowww.estec.esa.nl/users/expl_lib/PHT/c200fpsf02.ps.gz.

TABLE 1

ISO AND *IRAS* FLUXES

	F_{ISO}(60 μm)			F_{ISO}(90 μm)			F_{IRAS}		
STAR	Center (Pixel)	Boundary (Pixel Sum)	Background (Average)	Center (Pixel)	Boundary (Pixel Sum)	Background (Average)	12 μm	25 μm	60 μm
HD 119853.....	0.289 ± 0.089	0.509 ± 0.185	1.315 ± 0.059	0.187 ± 0.071	0.229 ± 0.229	1.047 ± 0.049	2.360	0.571	0.887
HD 221776.....	0.271 ± 0.045	0.293 ± 0.095	0.630 ± 0.025	0.177 ± 0.061	0.813 ± 0.112	0.691 ± 0.049	5.080	1.360	0.840
HD 153687.....	1.288 ± 0.127	1.543 ± 0.414	1.253 ± 0.069	0.755 ± 0.103	0.669 ± 0.478	1.349 ± 0.053	13.700	4.160	5.120
HD 156115.....	0.265 ± 0.107	0.225 ± 0.194	1.648 ± 0.071	0.221 ± 0.103	0.351 ± 0.191	1.786 ± 0.060	8.900	2.280	0.913
HD 202418.....	0.305 ± 0.036	0.477 ± 0.135	0.411 ± 0.019	0.218 ± 0.040	0.444 ± 0.173	0.558 ± 0.022	2.400	0.696	0.919
HD 218559.....	0.157 ± 0.036	0.320 ± 0.073	0.406 ± 0.028	0.107 ± 0.030	0.280 ± 0.066	0.482 ± 0.018	3.570	0.977	0.580
HD 212320.....	0.172 ± 0.083	0.221 ± 0.080	1.475 ± 0.045	0.180 ± 0.062	0.436 ± 0.109	1.007 ± 0.037	1.300	0.422	0.606
HD 19745	0.255 ± 0.034	0.133 ± 0.083	0.314 ± 0.025	0.220 ± 0.030	−0.034 ± 0.054	0.298 ± 0.020	0.296	0.777	0.612
HD 24124	0.000 ± 0.025	0.145 ± 0.114	0.351 ± 0.021	0.034 ± 0.021	0.352 ± 0.293	0.283 ± 0.016	0.334	0.250	0.400
HD 111830.....	0.395 ± 0.044	0.127 ± 0.100	0.505 ± 0.022	0.337 ± 0.058	0.398 ± 0.170	0.776 ± 0.034	0.571	0.231	0.972
HD 92253	0.158 ± 0.032	0.137 ± 0.062	0.439 ± 0.019	0.139 ± 0.049	0.198 ± 0.117	0.770 ± 0.031	0.774	0.223	0.604
HD 32440	0.237 ± 0.033	0.155 ± 0.095	0.356 ± 0.021	0.154 ± 0.027	0.073 ± 0.076	0.444 ± 0.011	8.000	2.000	0.573

NOTES.—Values are in units of janskys. Fluxes are non–color corrected. Central-pixel and sum of boundary-pixel fluxes are listed in the second and third and fifth and sixth columns for the 60 and 90 μm images, respectively. The background intensity, in an average background pixel, that was subtracted from the "on"-source fluxes is given in the fourth and seventh columns. The *IRAS* 12, 25, and 60 μm source fluxes are from the Faint Source Catalog. The boundary pixel to the south in the HD 221776 90 μm source image, which has the 90 μm out-of-center peak intensity, was not considered at 90 μm when deriving its boundary-pixel flux.

footprint values only at a few locations in the focal plane. Thus, one has to modify the PIA model footprint so that it best matches the Laureijs calibration. We find that shrinking the x-y scale (focal plane scale) of the model PIA footprint by 15% can well fit the observed footprint values. We choose altering the x-y scale of the model footprint instead of dividing all footprint values by a certain constant because the former also gives good fits to the ratios of observed footprints while the latter does not.

Here we assume two simple models for the distribution of the material responsible for excess far-IR emission: (1) an infinitesimally thin shell around the central star with an angular radius of θ_{ex}, appropriate for the orbiting and ejected circumstellar dust models, and (2) uniform distribution of material centered on the star with an angular radius of θ_{ex}, appropriate for the cirrus hot spot model (see § 1 and Jura 1999 for a detailed description of the orbiting dust, ejected dust, and cirrus hot spot models). Then r_{mod} is a ratio of the footprint convolved with the assumed distribution with a given θ_{ex} for the central pixel (f_c) to that for the sum of the boundary pixels (f_b):

$$r_{mod}(\theta_{ex}) \equiv \frac{f_c(\theta_{ex})}{f_b(\theta_{ex})} . \quad (1)$$

For the shell distribution model, the footprint is convolved with the projected distribution of a shell of constant intensity. In the case of a uniform distribution, the footprint is convolved with the projected distribution of a filled dust sphere with a radial intensity profile appropriate for an optically thin, equilibrium approximation.[4] The calculated $r_{mod}(\theta_{ex})$ is presented in Figure 2.

[4] See Appendix B of Sopka et al. (1985) for the radial intensity profile. The intensity profile is basically a Planck function with a local temperature given by their equation (B3), which is proportional to $R^{-2/(4+p)}$, where R is the distance from the star and p is the emissivity index. We adopt $p = 1.5$ following Jura (1999) and assume that the photospheric emission from the central star follows a Planck function as well.

The observed fluxes also include a contribution from the photosphere of the central star. Following Jura (1999), we estimate the photospheric emission from the star at 60 μm using the *IRAS* 12 μm flux and an assumed photospheric ratio $F^*(60)/F^*(12)$ of 0.0371 (Jura obtained this value by averaging the *IRAS* colors of the nine brightest K and G giants in the Yale Bright Star Catalogue). When converting the estimated *IRAS* photospheric flux for the *ISO* filters, we adopt color correction factors for a 4000 K blackbody. The 90 μm photospheric flux is extrapolated from the 60 μm photosphere with a blackbody assumption. The photosphere emission at 60 and 90 μm is assumed to be not diluted by the presence of a circumstellar shell. The estimated photospheric fluxes are given in Table 2. The contribution of the central star to the flux in each pixel can then be determined from the footprint, and we subtract these photospheric fluxes from the observed fluxes to determine the excess flux F^{ex} and r_{obs}:

$$r_{obs} \equiv \frac{F_c - P_c F^*}{F_b - P_b F^*} = \frac{F_c^{ex}}{F_b^{ex}} , \quad (2)$$

where F is the observed source flux, F^* is the estimated photospheric flux, P is the fraction of the flux that falls onto the central pixel or boundary pixels from a point source located at the center of the array, and the subscripts c and b are for the center and boundary pixels, respectively. P_c and P_b values, adopted from the modified PIA footprint model, are 0.66 and 0.12 for 60 μm and 0.59 and 0.15 for 90 μm, respectively (the rest of the flux falls outside the array). The variables for the boundary pixels are summed over the 8 pixels.

The angular size of the extended emission source, θ_{ex}, can be obtained from equating r_{mod} and r_{obs}. We find θ_{ex} that satisfy $r_{mod}(\theta_{ex}) = r_{obs}$ for both a shell and a uniform source distribution. The size of the extended emission source, R_{ex}, then follows from this θ_{ex} and the *Hipparcos*-measured dis-

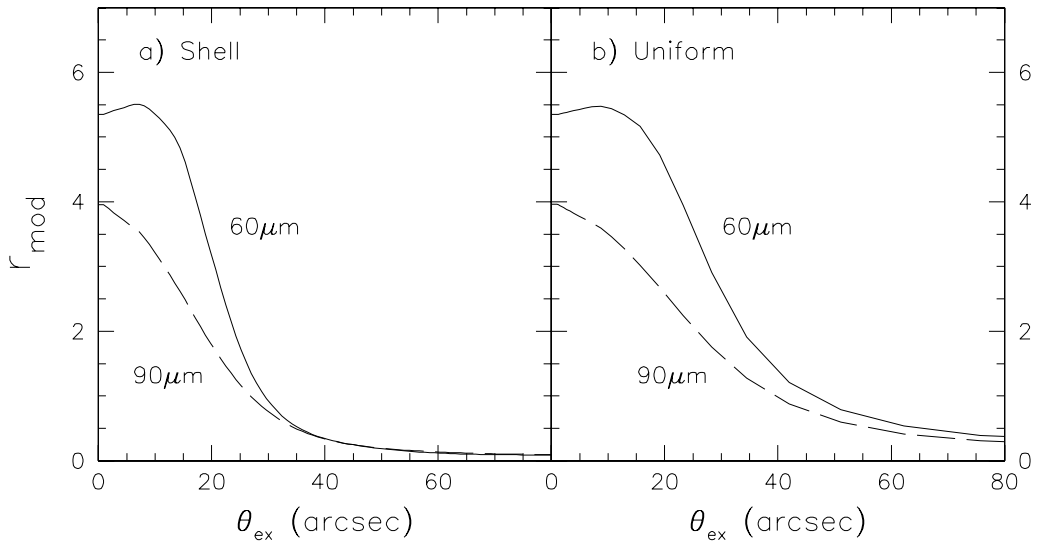

FIG. 2.—Modeled intensity ratio of central to boundary pixels of the *ISO* C100 camera, r_{mod}, for the extended, excess far-IR emission source at 60 (*solid lines*) and 90 μm (*dashed lines*) for (*a*) an infinitesimally thin shell of circumstellar matter with an angular radius of θ_{ex} and (*b*) a uniform distribution of cirrus material with an angular radius of θ_{ex}. In the case of the latter, the intensity ratio is a function of central star's parameters, D_*, T_*, and R_*. The intensity ratio shown in (*b*) is for HD 119853. The term r_{mod} has an initial rise near $\theta_{ex} = 0''$ at 60 μm whose existence is a result of the detailed shape of the footprint.

TABLE 2

COLOR-CORRECTED PHOTOSPHERIC FLUXES

Star	$F^{*,cc}(25)$	$F^{*,cc}(60)$	$F^{*,cc}(90)$
HD 119853.....	0.393	0.067	0.030
HD 221776.....	0.845	0.144	0.065
HD 153687.....	2.280	0.388	0.174
HD 156115.....	1.481	0.252	0.114
HD 202418.....	0.399	0.068	0.031
HD 218559.....	0.594	0.101	0.045
HD 212320.....	0.216	0.037	0.016
HD 19745	0.049	0.008	0.004
HD 24124	0.056	0.009	0.004
HD 111830.....	0.095	0.016	0.007
HD 92253	0.129	0.022	0.010
HD 32440	1.331	0.227	0.102

NOTE.—Values are in units of janskys.

tance to the star, D_* (see Table 4). Derived R_{ex} values and their uncertainties for our targets are given in Table 3 as well as r_{obs}.

The θ_{ex} values found here for the shell distribution (see Table 3) range from 20″ to 40″ (30″ to 70″ for the uniform distribution), implying that we were able to deconvolve extended sources whose angular size is smaller than the 43″ 1 pixel size of the detector. Plets et al. (1997), whose work was similar to that of Zuckerman et al. (1995), state that most of their luminosity class III giants with excess far-infrared emission appear to be unresolved in *IRAS* scans at 60 μm. We have convolved the 60 μm *IRAS* PSF with the projected distribution of a shell with an angular radius of 30″, which is the typical angular size of extended emission sources derived in the present study, and found that the FWHM of the convolved distribution is only $\sim$15% larger than that of the PSF. This small difference is thought to be the reason that the sources in Plets et al. "look" unresolved. By deconvolving the *IRAS* PSF, Hawkins & Zuckerman (1991) were able to resolve some objects with an angular radius smaller than 30″ at 60 μm, but their objects mostly had relatively high fluxes (larger than a few janskys). Since our targets have fluxes 1–2 orders lower (mostly a fraction of $\sim$1 Jy), deconvolution of the *IRAS* data will not reliably resolve our targets (G. W. Hawkins 2000, private communication). Thus, the *ISO* images appear to be the only ones currently available that can resolve our targets in the far-IR.

3.3. *Robustness of Our Results*

We consider possibilities that could give a systematic bias to the derived source sizes. To estimate the effects of inaccurate background determination, we decrease and increase the background by 5%, which is the average background uncertainty, and recalculate the R_{ex} values. While the decrease of the background produces a 10%–20% increase in R_{ex}, the increase of the background results in negative F^{ex} values (at central or boundary pixel; a negative F^{ex} implies that the target flux is smaller than the estimated photospheric flux). Thus, while a systematic overestimation of the background, if any, will result in slight underestimation of R_{ex}, considerable underestimation of the background seems unlikely. Moreover, as shown in Table 1 and Figure 1, the uncertainty of the *ISO* background is only a few percent, and there is a good agreement between the *ISO* and *IRAS* data without a bias toward a particular observation, which suggests that a systematic over or underestimation in the *ISO* background determination is very unlikely. On the other hand, we find that our "second calibration" (dividing the source flux by the background flux pixel by pixel) has an effect of increasing R_{ex} values by only $\sim$15%.

The estimation of F^* also could be a possible cause of bias. Here we try two methods for estimating F^* that differ from the one used in § 3.2. The first method (method A of Zuckerman et al. 1995) estimates $F^*(12)$ using the empirical relation between $F^*(12)$ and V magnitude as a function of $B-V$ color from Waters, Coté, & Aumann (1987) and extrapolates to $F^*(60)$ and $F^*(90)$ for a blackbody spectrum. The second method (method B of Zuckerman et al. 1995) assumes that the *IRAS* 12 μm flux is photospheric (as in § 3.2) and extrapolates to $F^*(60)$ and $F^*(90)$ with a blackbody spectrum. The new F^* estimation with methods A and B gives a considerable change in R_{ex} only for HD 156115 and HD 32440, where F^* is more than one-third of the total source flux. Methods A and B give $\sim$10% larger F^* and result in a 10%–20% R_{ex} increase for these two stars. Thus, the method of estimating F^* will not significantly affect the R_{ex} values.

TABLE 3

OBSERVED AND DERIVED SIZE PARAMETERS

		SHELL (60 μm)		UNIFORM (60 μm)			SHELL (90 μm)		UNIFORM (90 μm)	
STAR	r_{obs} (60 μm)	θ_{ex} (arcsec)	R_{ex} (AU)	θ_{ex} (arcsec)	R_{ex} (AU)	r_{obs} (90 μm)	θ_{ex} (arcsec)	R_{ex} (AU)	θ_{ex} (arcsec)	R_{ex} (AU)
HD 119853.....	0.48 ± 0.23	36	4200^{+1000}_{-500}	66	7700^{+14400}_{-1400}	0.74 ± 0.80	30	$3500^{+\infty}_{-1000}$	46	$5300^{+\infty}_{-1700}$
HD 221776.....	0.62 ± 0.23	33	7000^{+1000}_{-600}	57	12000^{+3800}_{-1700}	0.56 ± 0.32	33	7000^{+2500}_{-1100}	53	11000^{+9100}_{-2200}
HD 153687.....	0.68 ± 0.19	33	4000^{+400}_{-200}	53	6500^{+1200}_{-700}	0.99 ± 0.72	27	3300^{+2000}_{-800}	39	4800^{+5100}_{-1300}
HD 156115.....	0.46 ± 0.44	36	$9300^{+\infty}_{-1600}$	71	$18100^{+\infty}_{-5500}$	0.43 ± 0.31	37	9400^{+6900}_{-1700}	62	$15800^{+\infty}_{-4000}$
HD 202418.....	0.55 ± 0.17	35	7100^{+800}_{-500}	63	12900^{+4100}_{-1600}	0.45 ± 0.19	36	7400^{+1700}_{-900}	60	12300^{+6900}_{-2100}
HD 218559.....	0.28 ± 0.09	43	7700^{+1200}_{-700}	151	$27100^{+\infty}_{-12200}$	0.28 ± 0.10	43	7700^{+1700}_{-800}	84	$15100^{+\infty}_{-3200}$
HD 212320.....	0.67 ± 0.41	33	4600^{+1600}_{-500}	56	7900^{+19300}_{-1600}	0.39 ± 0.17	38	5400^{+1200}_{-700}	65	9200^{+7100}_{-1600}
HD 19745	1.89 ± 1.20	24	12200^{+4100}_{-2100}	39	20000^{+21600}_{-5100}	...	...	...	...	...
HD 111830.....	3.07 ± 2.44	20	3200^{+2000}_{-3200}	28	4500^{+5900}_{-4500}	0.84 ± 0.39	29	4500^{+1100}_{-700}	45	7000^{+3000}_{-3100}
HD 92253	1.06 ± 0.52	29	5600^{+1100}_{-600}	48	9200^{+4700}_{-1600}	0.68 ± 0.46	31	6000^{+3200}_{-1100}	50	9600^{+46900}_{-2300}
HD 32440	0.63 ± 0.39	33	7300^{+2700}_{-900}	56	12200^{+30900}_{-2400}	1.51 ± 1.60	22	$4800^{+\infty}_{-2400}$	31	$6800^{+\infty}_{-3600}$

NOTES.—Uncertainties are at 1 σ level. The uncertainty of r_{obs} comes from the source fluxes, F_c and F_b, and the uncertainty of R_{ex} corresponds to that of θ_{ex}, which is propagated from r_{obs}. We do not apply our size analysis to 90 μm HD 19745 data because they have negative F_b. HD 24124 is not listed here because the far-IR emission near the star is thought to be due to a galaxy.

Inaccurate PSF or footprint could also affect our size analysis. As mentioned earlier, we used the model footprint modified for a recent recalibration by Laureijs based on real *ISO* data from the same C100 camera. Recalculation of R_{ex} with the original model footprint produces a change in the results of less than 20% [the footprint modification resulted in about a 50% increase in $r_{mod}(\theta_{ex} = 0)$, or P_c/P_b, but the change in r_{mod} near the r_{obs} values of our targets due to the modification was relatively small]. Thus, unless the focal plane scale of the true footprint is largely different from that of the adopted footprint, inaccuracy in the adopted footprint is expected not to considerably affect our derived R_{ex}.

4. DISCUSSION

Jura (1999) estimated the extent of the circumstellar material around eight nearby giants with infrared excess using three source models. Since the models result in sizes that differ from each other by almost an order of magnitude, the size of the infrared excess source may be used to judge which model is most consistent with the observations.

Jura's models require the temperature and radius of the target star (T_*, R_*) and the temperature of the circumstellar grains (T_{ex}). T_* is obtained from the $B-V$ color, and R_* is inferred from T_*, distance to the star D_*, and V magnitude (see Table 4). Flower's (1996) conversion between $B-V$ color and T_* and the assumption that $M_{bol}(\mathrm{Sun}) = 4.74$ (Bessel, Catelli, & Plez 1998) are used in the above calculation.

To estimate T_{ex}, excess far-IR fluxes at two passbands are fitted by $\nu B_\nu(T_{ex})$ for the ejected dust model and by $B_\nu(T_{ex})$ for the orbiting dust model, where B_ν is the Planck function and ν is the frequency (see Jura 1999). Both *IRAS* and *ISO* data were used for the fitting, but we fit the *IRAS* data (25 and 60 μm) and the *ISO* data (60 and 90 μm) separately because the two observations have different beam sizes. For the *IRAS* data, excess fluxes are calculated with assumed photospheric ratios $F^*(25)/F^*(12) = 0.233$ and $F^*(60)/F^*(12) = 0.0371$. For the *ISO* data, we obtain the excess fluxes by subtracting the photospheric flux calculated in § 3.2 from the total flux. The T_{ex} values derived from the two data sets are each shown in Table 4. We use the average of the two for further analysis.

Jura's estimation for model source sizes are then given by

$$R_{ex}\begin{cases} 0.5\, R_*\left(\dfrac{T_*}{T_{ex}}\right)^2 & \text{for orbiting dust,} \\ 0.5\, R_*\left(\dfrac{T_*}{T_{ex}}\right)^{2.5} & \text{for ejected dust,} \\ 120\, R_*\left(\dfrac{kT_*}{h\nu}\right)^{2.75} & \text{for cirrus hot spot.} \end{cases} \quad (3)$$

Note that R_{ex} for the cirrus hot spot model is the radius at which half the energy is emitted. Table 5 gives model R_{ex} for our giants obtained by the above equations. Each model results in R_{ex} that differ by an order of magnitude, and only the cirrus model gives R_{ex} dependent on the wavelength.

Orbiting dust and ejected dust model R_{ex} values are to be compared to R_{ex} values derived from observed r_{obs} with an assumption of the shell distribution for the excess emission source, whereas the cirrus hot spot model R_{ex} values are to be compared to those derived with an assumption of the uniform distribution for the excess emission source (see Table 3 for the R_{ex} derived from the observations).

The region of 60 and 90 μm emission in the orbiting dust (Kuiper belt) model (Table 5) would be spatially unresolved with the C100 detectors. But Table 3 and Figure 2 indicate that the 60 and 90 μm emission regions of our target stars are resolved with typical angular radii greater than 20″. Thus, if the assumption of large (blackbody) grains in the Kuiper belt is appropriate, then the C100 data imply that the observed far-IR emission is not due to orbiting dust. If particles generated in a Kuiper belt structure are so small as to not radiate like blackbodies, then the expected far-IR source size could be consistent with the observed sizes. However, as noted by Jura (1999), small particles will be blown out of the systems by radiation pressure and would have to be consistently replenished. Then the dust masses required over the lifetime of the phenomenon would be very large (see Jura 1999).

TABLE 4

MODEL PARAMETERS

STAR	SPECTRAL TYPE	m_V (mag)	$B-V$ (mag)	D_* (pc)	$\lvert b\rvert$ (deg)	L ($L_\odot$)	T_* (K)	R_* ($\times 10^{12}$ cm)	$T_{ex,1}$ *IRAS* (K)	$T_{ex,1}$ *ISO* (K)	$T_{ex,2}$ *IRAS* (K)	$T_{ex,2}$ *ISO* (K)
HD 119853.....	G8 III	5.50	0.90	116	48	8.69×10^1	5050	0.85	54	116	47	68
HD 221776.....	K7 III	6.18	1.59	208	22	4.51×10^2	3800	3.43	87	90	70	59
HD 153687.....	K4 III	4.82	1.48	123	22	3.86×10^2	4020	2.83	81	141	67	74
HD 156115.....	K5 III	6.52	1.45	255	13	3.24×10^2	4070	2.53	94	48	75	38
HD 202418.....	K3 III	6.42	1.41	204	30	2.10×10^2	4140	1.97	77	96	64	61
HD 218559.....	K4 III	6.43	1.50	179	35	1.95×10^2	3980	2.05	91	76	73	53
HD 212320.....	G6 III	5.92	1.00	141	50	9.53×10^1	4840	0.97	82	61	67	46
HD 19745	K1 III	9.10	1.05	500	46	6.67×10^1	4770	0.84	148	81	104	55
HD 24124	K1 III	8.45	1.31	505	48	1.69×10^2	4300	1.64	100	...	79	...
HD 111830.....	K0 III	7.78	1.25	156	15	2.77×10^1	4400	0.63	69	82	58	56
HD 92253	K0 III	7.42	1.19	192	15	5.43×10^1	4500	0.85	65	75	55	53
HD 32440	K4 III	5.47	1.52	218	34	7.39×10^2	3950	4.06	104	66	81	48

NOTES.—This table is similar to Table 1 of Jura 1999. The term $\lvert b\rvert$ is the absolute galactic latitude, L is the bolometric luminosity, and $T_{ex,1}$ and $T_{ex,2}$ are the grain temperatures for the orbiting dust and the ejected dust models, respectively. The other parameters are defined in the text. HD 153687 (30 Oph) and HD 212320 (HR 8530) are also included in Jura's list. The values of m_V, $B-V$, and D_* are from the *Hipparcos* catalog except for HD 19745, for which the magnitudes in the Tycho catalog were adopted and D_* was determined photometrically with $M_V = 0.6$. T_{ex} from the *ISO* data of HD 24124 is not given because its peak intensity is not on the central pixel.

TABLE 5

MODEL R_{ex} OF TARGET STARS

Star	Orbiting	Ejected	Cirrus (60)	Cirrus (90)
HD 119853.....	100	2100	29000	88000
HD 221776.....	210	3000	53000	160,000
HD 153687.....	120	2300	51000	160,000
HD 156115.....	310	4200	47000	140,000
HD 202418.....	150	2400	39000	120,000
HD 218559.....	150	2200	36000	110,000
HD 212320.....	150	2200	29000	89000
HD 19745	48	780	24000	74000
HD 24124	100	1200	36000	110,000
HD 111830.....	72	1100	15000	45000
HD 92253	120	1800	21000	64000
HD 32440	300	4000	70000	210,000

NOTE.—Values are in units of AU.

Given the substantial uncertainties in the measured ratios for R_{ex} (Table 3), based on the ISOPHOT data, we are unable to choose between the mass ejection and cirrus hot spot models (uncertainties in R_{ex} are asymmetrical and larger toward the positive direction). The reason is that the uncertainties of r_{obs} are substantial, while the difference between values of r_{mod} calculated for these two models is not large. Thus, to choose between them one must fall back on the types of arguments given by Jura (1999). Unfortunately, such arguments support neither model particularly well.

Jura (1999) argued against the sporadic dust ejection model for two reasons: (1) a recent ejection of matter would give $F^{ex}(25)$ larger than $F^{ex}(60)$, but no K or late G giants within 300 pc of the Sun show $F^{ex}(25) > F^{ex}(60)$; and (2) one of the giants with far-IR excess, δ And (HD 3627), is apparently expanding at $v_{cs} \sim 300$ km s^{-1} (Judge, Jordan, & Rowan-Robinson 1987), implying only 20 yr for the dust to reach its estimated R_{ex}, but none of the stars analyzed by Jura (1999) show significant variability due to the expected dimming of starlight by the dust for the first few months. However, we find that eight out of 92 giants in the list presented by Zuckerman et al. (1995) have $F^{ex}(25) > F^{ex}(60)$. This frequency agrees with our simple calculation of $F^{ex}(25) - F^{ex}(60)$ evolution following the detachment of a thin shell, composed of dust with vB_v emissivity, from the photosphere with constant expansion velocity. Furthermore, we note that δ And is an unusual K giant. It is classified as a "hybrid star" that possesses both a 10^{6-7} K hot corona and a cool stellar wind (see Haisch, Schmitt, & Rosso 1992 and references therein), and Judge et al. (1987) suggested that the high-velocity wind from δ And may not be responsible for the formation of the circumstellar shell around the star. If the dust shell is assumed to be blown away at v_{cs} comparable to that of the stellar wind of asymptotic giant branch stars (a few tens of kilometers per second), one would have a much lower possibility of finding significant starlight variability in a given period.

Very recently, Kalas et al. (2001) conducted coronagraphic optical observations of 60 Vega-like stars (main-sequence stars with apparent excess far-IR emission) and around five stars found reflection nebulae that resemble those in the Pleiades. This suggests the cirrus hot spot model for the origin of excess far-IR emission from those five stars. Similar coronagraphic observations for our target stars might help one in choosing between the mass ejection and cirrus hot spot models.

5. SUMMARY

We have analyzed far infrared imaging data of 12 luminosity class III stars with associated dust particles, observed with the C100 camera on *ISO*. Far-IR excess emission is associated with the central star for 11 targets, and the excess emission of only one target appears to be due to a galaxy. Thus, we conclude that most of the stars presented by Zuckerman et al. (1995) actually heat dust particles in their vicinity.

Three models of the origin of the circumstellar dust considered by Jura (1999) predict very different source sizes. To estimate the size of the far-IR emission source, we examined the flux ratio of the central to 8 boundary pixels of the 3×3 C100 array. In one model considered by Jura (1999), the observed dust is produced as "Kuiper belt–like" materials located within a few hundred AU of the stars are warmed by the increasingly luminous giant star (the orbiting dust model). Such a far-IR–emitting region would appear spatially unresolved in the C100 images. But the observed emission regions do appear to be spatially resolved with radius at least a few thousand AU, and possibly significantly larger. With this size uncertainty, we are unable to choose between the other two models discussed by Jura—sporadic mass ejection and interstellar cirrus hot spot. Neither of these models is in particularly good agreement with all existing data (see, e.g., Jura 1999), so a clear choice between them (or other models) awaits additional observations, perhaps with *SIRTF* and/or ground-based optical coronographs.

We are grateful to Carlos Gabriel and Rene Laureijs of the ESA-VILSPA, Nanyao Lu of IPAC, and Celeste Spangler for helping us with the *ISO* data analysis. We thank Eric Becklin and Mike Jura for helpful discussion and reading the manuscript. The ISOPHOT data presented in this paper were reduced using PIA, which is a joint development by the ESA Astrophysics Division and the ISOPHOT Consortium. We have used the SIMBAD database, ALADIN sky atlas, and NED skyplot.

REFERENCES

Bessel, M. S., Catelli, F., & Plez, B. 1998, A&A, 333, 231
Flower, P. J. 1996, ApJ, 469, 355
Gabriel, C., Acosta-Pubildo, J., Heinrichsen, I., Morris, H., & Tai, W.-M. 1997, in ASP Conf. Ser. 125, Astronomical Data Analysis Software and Systems VI, ed. G. Hunt & H. E. Payne (San Francisco: ASP), 108
Haisch, B., Schmitt, J. H. M. M., & Rosso, C. 1992, ApJ, 388, L61
Hawkins, G. W., & Zuckerman, B. 1991, ApJ, 374, 227
Hoffleit, D., & Warren, W. H., Jr. 1991, The Bright Star Catalogue, 5th rev. ed. (New Haven: Yale Univ. Obs.)
Houk, N., Cowley, A. P., & Smith-Moore, M. 1975-1988, Michigan Spectral Catalogue, Vols. 1-4 (Ann Arbor: Univ. Michigan)
Judge, P. G., Jordan, C., & Rowan-Robinson, M. 1987, MNRAS, 224, 93
Jura, M. 1999, ApJ, 515, 706
Kalas, P., Graham, J., Jewitt, D., & Lloyd, J. 2001, ApJ, in press
Plets, H., Waelkens, C., Oudmaijer, R. D., & Waters, L. B. F. M. 1997, A&A, 323, 513
Sopka, R. J., Hildebrand, R., Jaffe, D. T., Gatley, I., Roellig, T., Werner, M., Jura, M., & Zuckerman, B. 1985, ApJ, 294, 242
Waters, L. B. F. M., Coté, J., & Aumann, H. H. 1987, A&A, 172, 225
Zuckerman, B., Kim, S. S., & Liu, T. 1995, ApJ, 446, L79